

## Temperature and Strain Effects in Micro-Raman Thermometry for Measuring In-Plane Thermal Conductivity of Thin Films

Shouyuan Huang, Yijie Chen, Zhe Luo & Xianfan Xu

To cite this article: Shouyuan Huang, Yijie Chen, Zhe Luo & Xianfan Xu (2021): Temperature and Strain Effects in Micro-Raman Thermometry for Measuring In-Plane Thermal Conductivity of Thin Films, Nanoscale and Microscale Thermophysical Engineering, DOI: [10.1080/15567265.2021.1912865](https://doi.org/10.1080/15567265.2021.1912865)

To link to this article: <https://doi.org/10.1080/15567265.2021.1912865>



Published online: 11 Apr 2021.



---

Submit your article to this journal [↗](#)



---

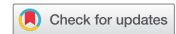
View related articles [↗](#)



---

View Crossmark data [↗](#)

---



# Temperature and Strain Effects in Micro-Raman Thermometry for Measuring In-Plane Thermal Conductivity of Thin Films

Shouyuan Huang<sup>#</sup>, Yijie Chen<sup>#</sup>, Zhe Luo<sup>\*</sup>, and Xianfan Xu

School of Mechanical Engineering and Birck Nanotechnology Center, Purdue University, West Lafayette, Indiana, USA

## ABSTRACT

Micro-Raman thermometry is an effective method for measuring thermal conductivity of thin films. It features noncontact and nondestructive probing and convenience of sample preparation. However, there is a concern of its accuracy when using the Raman peak shift as the temperature transducer since it responds to both temperature and strain upon optical heating. In this work, a series of detailed experiments are carried out to evaluate contributions to Raman signals from temperature only vs. from thermomechanical strain. It is shown that using proper calibration, contributions to Raman signals from temperature only and from thermomechanical strain can be decoupled and thermal conductivity can be evaluated correctly. These procedures are then applied to bismuth telluride thin films to illustrate measurement of thin film thermal conductivity.

## ARTICLE HISTORY

Received 16 February 2021

Accepted 29 March 2021

## KEYWORDS

Micro-Raman thermometry; thermal conductivity; thin film; optothermal Raman measurement technique; bismuth telluride

## Introduction

Raman scattering in solids reflects the information of certain phonon modes and can be calibrated as optical thermometry [1]. Since the laser used in Raman scattering can also serve as an optical heat source, the resulting temperature rise vs. Raman scattering can be used as a temperature transducer and the thermal conductivity can hence be extracted from heat conduction modeling. Contactless thermal conductivity measurement using micro-Raman thermometry was first demonstrated in 1999 [2, 3]. The in-plane thermal conductivity measurement of graphene [4, 5] reintroduced the micro-Raman technique to the thermophysical community, along with the flourish of thermal transport studies in 2D materials and nanometer-thin films in the last decades. The micro-Raman technique was then applied to the measurements of numerous thin films such as transition metal dichalcogenides [6–8], hexagonal BN [9], bismuth [10], aluminum oxide [10], black phosphorus [11, 12], tetradymites [13, 14], 2D-tellurium [15], and 2D ferromagnetic materials [16], owing to the particular advantage in measuring the in-plane thermal conductivity of nanometer-thin films. Since no additional temperature transducer is needed in this contactless method, the loss of resolution due to shunting of heat flow is avoided. The convenience of sample preparation is another advantage over the well-accepted electrothermal microbridge method [17, 18]. The capability of the micro-Raman method can also be expanded to transient measurements using ultrafast laser spectroscopy and to probe more detailed transport properties [19–25]. However, precautions are needed to perform reliable in-plane thermal conductivity measurements when using the micro-Raman technique. One example is that nonequilibrium phonons may exist even in steady-state measurement [26, 27], and Raman scattering with these modes should not be directly used as the temperature transducer. The temperature and

**CONTACT** Xianfan Xu  [xxu@ecn.purdue.edu](mailto:xxu@ecn.purdue.edu)  School of Mechanical Engineering, Purdue University, 585 Purdue Mall, West Lafayette, IN 47907.

<sup>\*</sup>Present address: Pure Storage, Mountain View, California, USA

<sup>#</sup>These authors contributed equally to this work

strain effects during the in-plane thermal conductivity measurement using the Raman method are another concern, and are the major focus of this work.

In micro-Raman measurements, it is a common practice to use the temperature-dependent Raman peak shift, i.e. the shift of the lattice vibrational frequency, as the temperature transducer. Due to the anharmonicity of the interatomic potential, the frequency shift responds to both temperature and strain in two ways [28]: The elongated atomic bonds are softened, resulting in a redshift of Raman peak responding to either mechanical stress or thermal expansion. Also, phonon–phonon interactions also contribute to the frequency shift (a pure temperature contribution, sometimes called the explicit contribution [28]), namely, the interatomic potential can be tailored by lattice vibrational energy changes, arising from the altered phonon population per Bose–Einstein distribution at varying temperatures. This combined effect has been applied to map the temperature and strain distribution in, e.g., power electronic or piezoelectric devices directly and simultaneously [29–31]. On the other hand, this temperature and strain complexity leads to concerns on the accuracy of the Raman-temperature transducer. This will be described with a brief review of the operation procedure for thermal conductivity measurement as follows. The sample is first placed in a thermal bath at varied temperatures and its Raman shift is monitored, with minimal laser incident power to reduce optical heating. The Raman shift vs. bath temperature is then fitted using a linear function and the fitted slope is calibrated as the Raman-temperature coefficient  $\chi_T = d\omega/dT$ . During thermal conductivity measurement, the laser heats the center of the suspended sample, and the Raman signal/shift is collected to indicate the temperature of the laser heated spot using the calibrated Raman-temperature coefficient. Thermal conductivity is then extracted using heat conduction modeling. Detailed procedures can be found in earlier works [10, 11, 13]. Here, it is important to understand that the temperature coefficient may vary for the sample at different mechanical states, i.e., when the sample is suspended or supported on a substrate. Furthermore, even if the temperature calibration and the thermal conductivity measurement are performed with the laser focused at the same spot of the suspended region (Figure 1a), there is still a question if this “suspended Raman temperature coefficient” obtained when the entire sample is uniformly heated in the thermal bath during calibration, can be used when locally heated during the thermal conductivity measurement, since the strain distribution in these two cases can be different.

In this work, we study the in-plane thermal conductivity measurement using a well-studied material, exfoliated thin-film  $\text{Bi}_2\text{Te}_3$  [32–38] as an example to evaluate the temperature and strain effects in micro-Raman thermometry using a series of thermal and mechanical calibrations. We found that the measured Raman shift can be simply expressed as the linear summation of pure-temperature and thermomechanical contribution, and the higher-order terms are confirmed negligible within the

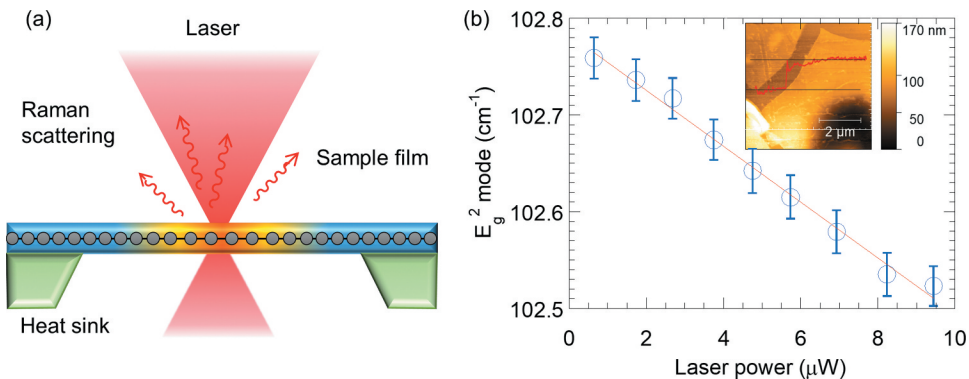


**Figure 1.** Optothermal micro-Raman measurement of thin film in-plane thermal conductivity (a) Schematic of laser focusing at the center of the suspended thin film sample, locally heating inducing Raman scattering as temperature transducer, also resulting in local thermal expansion. (b) Raman shift ( $E_g^2$  mode selected as Raman transducer) vs. incident laser power of a 16-nm thin film  $\text{Bi}_2\text{Te}_3$ . Inset: atomic force microscope image of the  $\text{Bi}_2\text{Te}_3$  film.

range of uncertainty. Lastly, we present the in-plane thermal conductivity measurement of  $\text{Bi}_2\text{Te}_3$  thin films. The results address the temperature vs. strain effects and validate the operation procedure of micro-Raman technique for in-plane thermal conductivity measurement.

## Experiment results and discussion

$\text{Bi}_2\text{Te}_3$  thin films are tape-exfoliated from the bulk crystals grown using the Bridgman method [39]. For thermal conductivity measurement, the thin film is suspended on holey SiN membranes using the PVA/PMMA wet transfer technique [11, 13, 40–42]. The micro-Raman measurement is performed at room temperature in a nitrogen environment. A 633-nm He-Ne laser with controlled incident power is focused (Olympus MPLN 100 $\times$ , NA = 0.90) at the center of the suspended region. The laser heating locally elevates the temperature and the heat is mostly dissipated in-plane toward the SiN heat sink, creating a temperature gradient as shown in Figure 1a. The Raman spectra is obtained using a spectrometer with groove density of 1800  $\text{mm}^{-1}$  giving a spectral resolution of 0.27  $\text{cm}^{-1}$ . The Raman peak of  $E_g^2$  mode is selected as the temperature transducer due to the higher sensitivity (large Raman-temperature coefficient). Its dependence on the incident power is plotted in Figure 1b and can be linearly fitted with  $R^2 > 0.99$ . Presuming that the  $E_g^2$  mode Raman peak serves as a temperature transducer, Figure 1b can be interpreted into a relation of local temperature rise vs. laser heating. Subsequently, the in-plane thermal conductivity of the thin film can be extracted from a heat conduction model. Temperature rise due to the minimal laser can be quantified using the calibrated Raman temperature transducer (showed below), and in our case is less than 1 K.

Now we address the validity of the Raman-temperature calibration for the mechanical condition of suspended film. We consider a general case of Raman shift with coexisting temperature rise and mechanical strain. In the following discussion on Raman coefficients, we use  $\zeta$  for the material properties in theory, and  $\chi$  for the experimental measurables. The total Raman shift  $\Delta\omega$  can be written as in Equation (1).  $\zeta_T$  is the pure temperature coefficient or the Raman-temperature coefficient with lattice constants fixed with respect to the value at room temperature, referred to as “strain free,” and  $\zeta_\varepsilon$  is the Raman-strain coefficient for uniaxial strain; and  $\alpha$  is the thermal expansion coefficient.  $\sigma_i$  is the mechanical stress applied in the  $i$ -axis, and  $E$  is Young’s modulus, and  $\nu$  is the Poisson ratio. The first term on the right-hand side is the Raman shift of pure temperature contribution (only due to the phonon–phonon interactions). The parentheses summarize the total (hydrodynamic) strain. The first term in the parentheses is the Raman shift due to thermal expansion, and the second term is the response to the normal mechanical strains. The last term represents the higher-order and covariant terms, which are expected to be negligible for small perturbations. We will also empirically show that it is indeed negligible.

$$\Delta\omega = \zeta_T\Delta T + \zeta_\varepsilon \sum_i \left( \alpha_i\Delta T + \sigma_i \frac{(1-\nu)}{E} \right) + o(T, \varepsilon) \quad (1)$$

The thermal expansion coefficient of SiN ( $3.3 \times 10^{-6} \text{ K}^{-1}$ ) is smaller than that of most of the thin-film materials (including bulk  $\text{Bi}_2\text{Te}_3 \sim 1.5 \times 10^{-5} \text{ K}^{-1}$  [36, 43]), thus the suspended films experience compression during both the uniform heating (calibration) and local heating cases. It is likely that the mechanical stress in suspended nanometer-thin films to be released due to buckling due to the large aspect ratio of thickness (tens of nm) and lateral size (several  $\mu\text{m}$ ). The critical buckling strain of circular suspended films can be estimated using the Euler’s stability formula of drum surfaces in Equation (2) [44], where  $\nu$  is the Poisson ratio of the suspended film ( $\sim 0.2$  for  $\text{Bi}_2\text{Te}_3$ ),  $t$  is the thickness, and  $R$  is the radius of the circular suspension region. Taking the  $\text{Bi}_2\text{Te}_3$  thin films reported in this work (6–30 nm) as an example, the critical buckling strain is estimated to be  $\sim 2 \times 10^{-6}$ – $5 \times 10^{-5}$ , corresponding to the thermal expansion from a temperature rise of 0.15–4 K. Hence the suspended thin film samples achieve stress-free during the optothermal Raman tests with a typical temperature rise of tens of Kelvins in the experiments.

$$\varepsilon_c = \frac{2.16^2}{12(1-\nu^2)} \left(\frac{t}{R}\right)^2 \quad (2)$$

In this suspension and buckling scenario, Equation (1) can be simplified to Equation (3), describing the free thermal expansion. It is worth noticing that this reorganizing of terms introduces another Raman-temperature coefficient at the stress-free condition  $\chi_{T,\sigma=0}$  shown in Equation (3) which is defined by the material properties  $\zeta_T$ ,  $\zeta_\varepsilon$ , and  $\alpha$ . The definition of  $\chi_{T,\sigma=0}$  is hence not specified to the detailed strain distribution, but is applicable as long as the film is stress-free. The Raman-temperature coefficient calibrated at the center of the suspension region  $\chi_T$  is in essence the stress-free Raman temperature coefficient defined here.

$$\Delta\omega = (\zeta_T + 2\zeta_\varepsilon\alpha)\Delta T = \chi_{T,\sigma=0}\Delta T \quad (3)$$

Next, we confirm the linearity and decoupling of the Raman coefficients before the suspended  $\chi_T$  can be confidently used in the thermal conductivity measurement. We present below a systematic series of calibrations to show that the Raman responses of temperature and strain are linear and the  $o(T, \varepsilon)$  terms in Equation (1) are negligible within the range during the thermal conductivity measurement. This series of studies consists of temperature calibration of thin-film samples supported on three different types of substrates, and a calibration using a mechanical bending test at room temperature.

Thin films are transferred onto fused silica, silicon, and sapphire substrates to perform the Raman-temperature calibration. The PDMS stamping method was used to peel and transfer the films from one substrate to another to maximize the consistency of the sample used. For each case, a few samples ranging from 10 to 30 nm are examined to account for the uncertainties due to sample-to-sample variation. The Raman thermometry is conducted for the samples immersed in a nitrogen environment and a thermal bath of temperature ranging from room temperature to  $\sim 100^\circ\text{C}$ , and one typical set of results are summarized in Figure 2. Figure 2a shows the peak shift of the  $E_g^2$  mode of which is selected to be the temperature coefficient. The Raman shift vs. bath temperature of the thin film supported on fused silica, silicon, and sapphire substrates are plotted and linear fitted in Figure 2b–d respectively. The Raman-temperature relations are all linear with  $R^2 > 0.98$ . It is seen that the (absolution value of) the Raman-temperature coefficients increase with the thermal expansion coefficients of the substrates. The thermal expansion coefficients (provided by the vendors) and the corresponding Raman-temperature coefficients are summarized in Table 1.

Raman measurements when  $\text{Bi}_2\text{Te}_3$  thin films supported on Si substrates are subject to mechanical uniaxial bending are performed using a home-made bending tool, as shown in Figure 3a. The strain is controlled using a pair of micrometers. The tensile strain on the top surface of the Si wafer ( $t = 525 \mu\text{m}$ ) can be calculated using the beam equation Equation (4) [45], where  $d_z$  is the deflection of the plate in the vertical direction,  $t$  is the wafer thickness, and  $a$  and  $L$  are the dimensions (nearest and farthest points) of the contact points of the bending tool. The Raman spectra of the  $\text{Bi}_2\text{Te}_3$  thin film at given calculated tensile strain are shown in Figure 3b. We again select the  $E_g^2$  mode of  $\text{Bi}_2\text{Te}_3$  as its Raman strain transducer, and the  $E_g^2$  mode Raman shift are fitted and plotted against the applied mechanical strain calculated from the micrometer readings as shown in Figure 3c. The linearity of Raman shift vs. strain relation, as shown in Figure 3c, leads to a constant Grüneisen parameter  $\gamma$  (Equation (5),  $\zeta_\varepsilon = \gamma\omega_0$ ) which is a signature of the no-slip condition during the mechanical bending tests [46]. According to Equation (1), the Raman strain coefficient obtained from the uniaxial bending test is  $\chi_\varepsilon = (1 - \nu_{\text{Si}})\zeta_\varepsilon$ . Using the Poisson ratio of silicon ( $\nu_{\text{Si}} = 0.25$ ) and the averaged slope in the uniaxial bending tests, the Raman-strain coefficient  $\zeta_\varepsilon$  is extracted to be  $-4.324 \text{ cm}^{-1}/\%$ . It is also confirmed that the no-slip interface condition by strain cycling that the Raman shift followed the same line as the tensile strain is released. We would also want to point out that there is no slip at the heterointerface of supported samples and the substrates during the temperature calibrations because the maximum strain applied in the bending test is greater than the differences of thermal expansion between sample and substrate. Furthermore, the Raman response of silicon is examined to verify the correctness of the applied strain. In Figure 3d, the uniaxial strains of the Si top surface calculated using

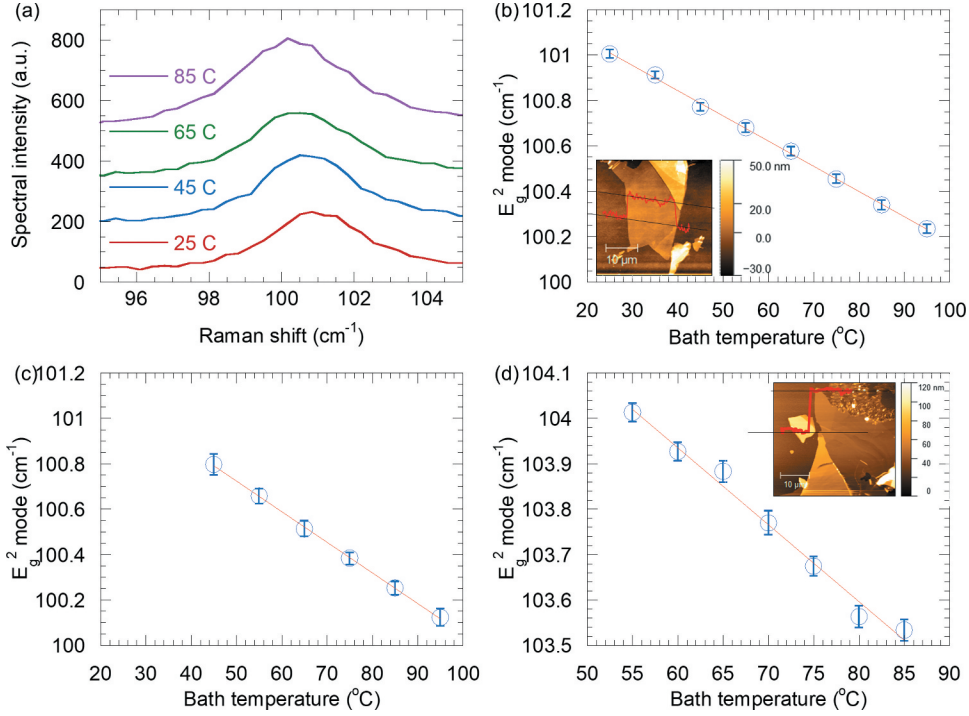


**Figure 2.** Raman thermometry: temperature calibration of Bi<sub>2</sub>Te<sub>3</sub> thin film supported on varied substrates (a) Raman spectra of Bi<sub>2</sub>Te<sub>3</sub> thin film under different temperature supported on fused silica. (b, c, d) Raman shift of E<sub>g</sub><sup>2</sup> mode vs. bath temperature of a 14-nm Bi<sub>2</sub>Te<sub>3</sub> film on (b) fused silica (c) silicon and of a 11-nm Bi<sub>2</sub>Te<sub>3</sub> film on (d) sapphire. Insets: atomic force microscope images of the Bi<sub>2</sub>Te<sub>3</sub> films.

**Table 1.** Thermal expansion coefficients and Raman-temperature coefficients of Bi<sub>2</sub>Te<sub>3</sub> thin film supported on substrates.

	$\alpha$ ( $\times 10^{-6}$ K <sup>-1</sup> )	$\chi_{T,s}$ (cm <sup>-1</sup> /K)
Fused silica	0.55	-0.0110
Silicon (100)	2.6	-0.0136
Sapphire (0001)	6.95	-0.0170

Equation (4) and the micrometer readings are compared with those extracted from the Raman shift. The strains obtained from the two methods can be linearly fitted with a < 7% discrepancy between their slopes. The Raman responses of Bi<sub>2</sub>Te<sub>3</sub> and Si are also plotted in Figure 3d and fall on one line. We hence validate that the strain is correctly applied to thin-film samples.

$$\varepsilon = \frac{3d_z t}{a(3L-4a)} \quad (4)$$

$$\gamma = -\frac{V}{\omega_0} \frac{\partial \omega_0}{\partial V} = -\frac{\Delta \omega_0}{\varepsilon_n \omega_0} = -\frac{\Delta \omega_0}{\varepsilon_{||} (1-\nu_{Si}) \omega_0} \quad (5)$$

Now we summarize the calibration data described above to show that the Raman responses to temperature and strain can be expressed as a linear combination, and the higher-order and covariance terms can be safely neglected during the thermal conductivity measurement. During the temperature rise in the thermal bath, the thin film samples experience isotropic strain according to the thermal expansion of the substrates. The Raman shift of the supported thin film on a certain substrate (subscript “s”) and the corresponding temperature coefficient  $\chi_{T,s}$  can thus be written as Equation 6 (a,b), which is a generalization of Equation (3). Performing the temperature calibration of the thin

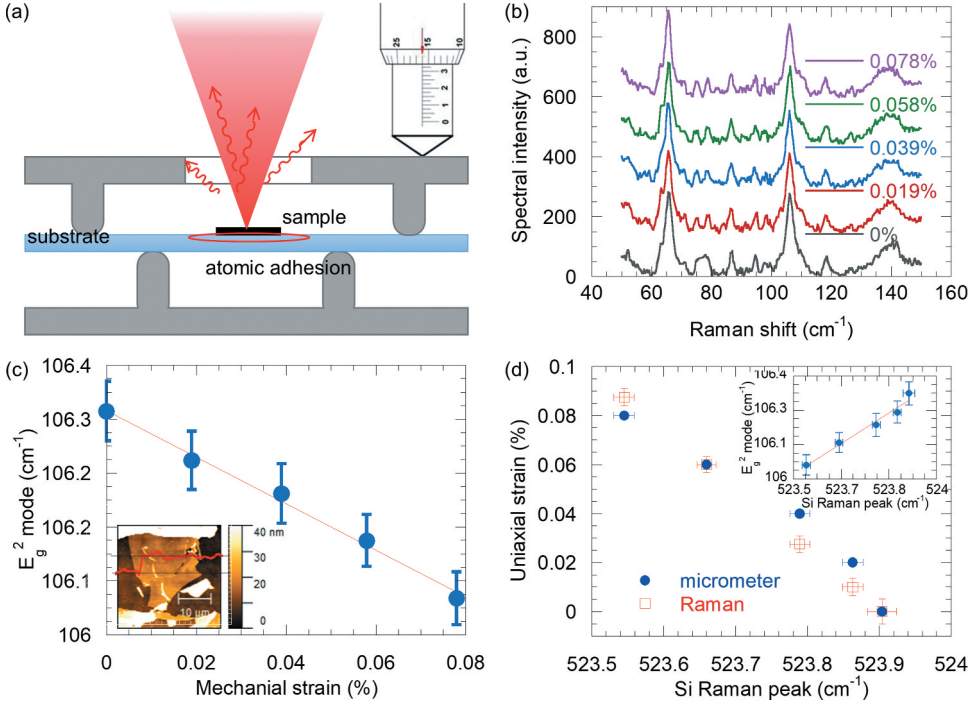


**Figure 3.** Raman response to uniaxial strain (a) Four-point bended thin film samples measured by Raman spectroscopy. (b) Raman spectra of Bi<sub>2</sub>Te<sub>3</sub> thin film under different temperatures supported on Si substrate. (c) Raman shift of E<sub>g</sub><sup>2</sup> mode of Bi<sub>2</sub>Te<sub>3</sub> thin film vs. mechanical uniaxial strain. Inset: atomic force microscope image of the Bi<sub>2</sub>Te<sub>3</sub> thin film. (d) The strain calculated from the micrometer and the strain extracted from Raman shift of silicon of the data points. inset: E<sub>g</sub><sup>2</sup> mode Raman shift of the Bi<sub>2</sub>Te<sub>3</sub> thin film vs. the corresponding Raman shift of silicon.

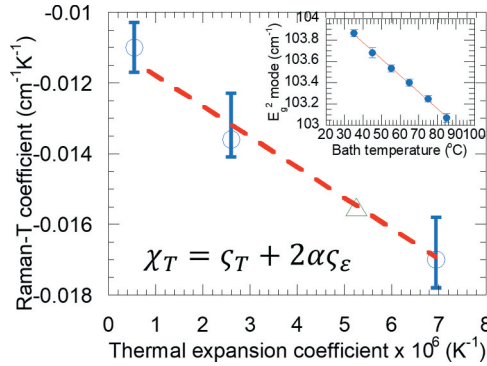


**Figure 4.** Summary of the Raman-temperature coefficient calibrated on substrates with different thermal expansion coefficients (blue circles) and fitted by the slope of Raman-(hydro) strain coefficient of  $2\zeta_\epsilon = -8.648 \text{ cm}^{-1}\%^{-1}$ . Inset: Raman shift of E<sub>g</sub><sup>2</sup> mode vs. bath temperature of suspended Bi<sub>2</sub>Te<sub>3</sub> thin film (temperature coefficient included in the main figure as the green triangle).

films on substrates with different thermal expansion coefficients provides additional data points and improves the fidelity of the strain-temperature decoupling. In Figure 4, we summarize the Raman-temperature coefficient obtained from samples supported on fused silica, silicon, and sapphire. The error bars represent the uncertainties due to sample-to-sample variation when multiple samples (ranging from 10 to 30 nm) were used. The fitted slope is very close to the Raman-(hydro)strain coefficient  $2\zeta_\epsilon$  (the factor of 2 comes from biaxial thermal expansion) as we suggested in Equation (3). Here we plot the (red dashed) fitting line with the slope prescribed as  $2\zeta_\epsilon$ , and the temperature

calibration results fall on this fitting line within the uncertainties. The temperature and strain calibration results in [Figure 4](#) hence show high fidelity of the superposition of the temperature and the strain effects, and the negligible higher-order/covariance terms within the experimental uncertainty. The result of calibration of a suspended film ([Figure 4](#) inset) is also included in [Figure 4](#) as the green triangle. The fact that the green triangle falls on the line indicates that expansion of the film is determined by its own thermal expansion, hence it is buckled to release stress. It is found that both thermal expansion determined by the substrate and intrinsic phonon–phonon interactions of the film contribute a significant percentage to the temperature-dependent Raman shift. The Raman temperature coefficients obtained from different substrates can vary by more than 50% from  $-0.011 \text{ cm}^{-1}/\text{K}$  to  $-0.017 \text{ cm}^{-1}/\text{K}$ , depending on thermal expansion of the substrate. On the other hand, the temperature calibration at the buckled suspended region associates neither with external material properties nor the local strain distribution. Hence in the thermal conductivity measurement, it is critical to use the temperature coefficient calibrated for the suspended film as the thermal transducer. The Raman-temperature coefficient of the suspended film can also be used to extract the thermal expansion coefficient of the thin film [47].

$$\Delta\omega = (\zeta_{T,\varepsilon=0} + 2\alpha_s\zeta_\varepsilon)\Delta T \quad (6a)$$

$$\chi_{T,s} = \zeta_T + 2\alpha_s\zeta_\varepsilon = \zeta_T + \frac{2\alpha_s\chi_\varepsilon}{1-\nu_{Si}} \quad (6a)$$

Based on the above discussions, the temperature calibration results  $\chi_{T,\sigma=0}$  at the center of the suspended region can be confidently used as the temperature transducer. We perform and analyze measurements for in-plane thermal conductivity of  $\text{Bi}_2\text{Te}_3$  thin film ranging from 10–30 nm. Both the temperature calibration and the thermal conductivity measurement (Raman shift vs. laser heating, e.g. [Figure 1b](#)) are performed with the laser focused at the center of the suspended region. Optical absorptivity is obtained from reflection/transmission measurements. A numerical heat conduction model is subsequently used to extract the in-plane thermal conductivity [10, 11, 13]. The extracted thermal conductivities are plotted in [Figure 5](#). A clear reduction of thermal conductivity from a near bulk value of  $\sim 3.5 \text{ W/mK}$  [35] is observed for films below 20 nm, to as low as  $\sim 2.5 \text{ W/mK}$  for  $\sim 10\text{-nm}$  samples. This is mainly attributed to the boundary scattering of the phonons due to boundary scattering [32, 34, 48]. Here we fit the thickness-dependent thermal conductivities considering the classical size effect using a simple equation  $\kappa = \frac{t}{(t+\lambda)}\kappa_b$  [49], while detailed calculations of thermal conductivity with size effect are outside the scope of this work. The phonon mean-free-path  $\lambda$  is fitted to be about 6 nm and the bulk thermal conductivity  $\kappa_b$  is fitted to about  $3.6 \text{ W/mK}$ .

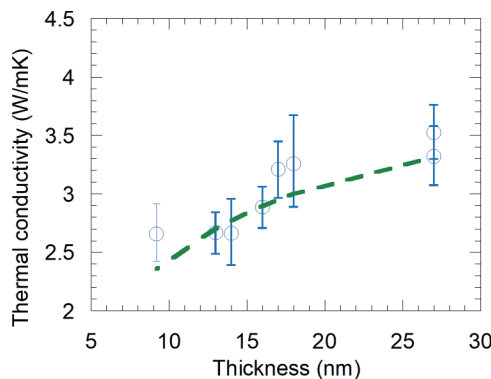


**Figure 5.** In plane thermal conductivity results of  $\text{Bi}_2\text{Te}_3$  thin films at varied thickness, fitted considering classical size effect with a mean-free-path of 6 nm.

To conclude, we used a series of testing and calibration procedures to study the complex temperature vs. strain response during optothermal micro-Raman measurements of in-plane thermal conductivity of thin films. These studies showed the Raman response to temperature and thermomechanical strains are both linear and can be superimposed. The stress-free Raman temperature coefficient can be defined which is not specific to detailed strain distribution. The results justified the Raman temperature coefficient obtained at the center of a suspended thin film as a valid temperature transducer for thin films with tens of nanometer thickness that experience buckling. On the other hand, our studies showed that the calibration performed on supported samples would fail to serve this purpose due to the thermal expansion of the substrate. We measured the thermal conductivity of Bi<sub>2</sub>Te<sub>3</sub> thin films, and the results showed strong suppression of thermal conductivity due to boundary scattering when the thickness was reduced.

## Acknowledgments

The authors thank Dr. I. Miotkowski and Prof. Y.P. Chen for providing the bulk material, and Prof. P.D. Ye for the bending tool. We also thank L. Zhang for valuable discussions.

## Funding

This work is partly supported by NSF EFMA-1641101.

## References

- [1] T. R. Hart, R. L. Aggarwal, and B. Lax, "Temperature dependence of Raman scattering in silicon," *Phys. Rev. B*, vol. 1, pp. 638–642, 1970. DOI: [10.1103/PhysRevB.1.638](https://doi.org/10.1103/PhysRevB.1.638).
- [2] S. Périchon, V. Lysenko, B. Remaki, D. Barbier, and B. Champagnon, "Measurement of porous silicon thermal conductivity by micro-Raman scattering," *J. Appl. Phys.*, vol. 86, pp. 4700–4702, 1999. DOI: [10.1063/1.371424](https://doi.org/10.1063/1.371424).
- [3] V. Lysenko, S. Perichon, B. Remaki, D. Barbier, and B. Champagnon, "Thermal conductivity of thick meso-porous silicon layers by micro-Raman scattering," *J. Appl. Phys.*, vol. 86, pp. 6841–6846, 1999. DOI: [10.1063/1.371760](https://doi.org/10.1063/1.371760).
- [4] A. A. Balandin *et al.*, "Superior thermal conductivity of single-layer graphene," *Nano Lett.*, vol. 8, pp. 902–907, 2008. DOI: [10.1021/nl0731872](https://doi.org/10.1021/nl0731872).
- [5] W. Cai *et al.*, "Thermal transport in suspended and supported monolayer graphene grown by chemical vapor deposition," *Nano Lett.*, vol. 10, pp. 1645–1651, 2010. DOI: [10.1021/nl9041966](https://doi.org/10.1021/nl9041966).
- [6] R. Yan *et al.*, "Thermal conductivity of monolayer molybdenum disulfide obtained from temperature-dependent Raman spectroscopy," *ACS Nano*, vol. 8, pp. 986–993, 2014. DOI: [10.1021/nn405826k](https://doi.org/10.1021/nn405826k).
- [7] R. Wang *et al.*, "Measurement of the thermal conductivities of suspended MoS<sub>2</sub> and MoSe<sub>2</sub> by nanosecond ET-Raman without temperature calibration and laser absorption evaluation," *Nanoscale*, vol. 10, pp. 23087–23102, 2018. DOI: [10.1039/C8NR05641B](https://doi.org/10.1039/C8NR05641B).
- [8] H. Zobeiri, *et al.*, "Frequency-domain energy transport state-resolved Raman for measuring the thermal conductivity of suspended Nm-Thick MoSe<sub>2</sub>," *Int. J. Heat Mass Transfer*, vol. 133, pp. 1074–1085, 2019. DOI: [10.1016/j.ijheatmasstransfer.2019.01.012](https://doi.org/10.1016/j.ijheatmasstransfer.2019.01.012).
- [9] H. Zhou *et al.*, "High thermal conductivity of suspended few-layer hexagonal boron nitride sheets," *Nano Res.*, vol. 7, pp. 1232–1240, 2014. DOI: [10.1007/s12274-014-0486-z](https://doi.org/10.1007/s12274-014-0486-z).
- [10] Z. Luo *et al.*, "Measurement of In-plane thermal conductivity of ultrathin films using micro-Raman spectroscopy," *Nanoscale Microscale Thermophys. Eng.*, vol. 18, pp. 183–193, 2014. DOI: [10.1080/15567265.2014.892553](https://doi.org/10.1080/15567265.2014.892553).
- [11] Z. Luo *et al.*, "Anisotropic in-plane thermal conductivity observed in few-layer black phosphorus," *Nat. Commun.*, vol. 6, pp. 1–32, 2015. DOI: [10.1038/ncomms9572](https://doi.org/10.1038/ncomms9572).
- [12] T. Wang, *et al.*, "Characterization of anisotropic thermal conductivity of suspended Nm-thick black phosphorus with frequency-resolved Raman spectroscopy," *J. Appl. Phys.*, vol. 123, pp. 145104, 2018. DOI: [10.1063/1.5023800](https://doi.org/10.1063/1.5023800).
- [13] Z. Luo *et al.*, "Large enhancement of thermal conductivity and Lorenz number in topological insulator thin films," *ACS Nano*, vol. 12, pp. 1120–1127, 2018. DOI: [10.1021/acsnano.7b06430](https://doi.org/10.1021/acsnano.7b06430).

- [14] P. Ghaemi, R. S. K. Mong, and J. E. Moore, "In-plane transport and enhanced thermoelectric performance in thin films of the topological insulators  $\text{Bi}_2\text{Te}_3$  and  $\text{Bi}_2\text{Se}_3$ ," *Phys. Rev. Lett.*, vol. 105, pp. 166603, 2010. DOI: [10.1103/PhysRevLett.105.166603](https://doi.org/10.1103/PhysRevLett.105.166603).
- [15] S. Huang *et al.*, "Anisotropic thermal conductivity in 2D tellurium," *2D Mater.*, vol. 7, pp. 015008, 2020. DOI: [10.1088/2053-1583/ab4ee4](https://doi.org/10.1088/2053-1583/ab4ee4).
- [16] F. Kargar *et al.*, "Phonon and thermal properties of quasi-two-dimensional  $\text{FePS}_3$  and  $\text{MnPS}_3$  antiferromagnetic semiconductors," *ACS Nano*, vol. 14, pp. 2424–2435, 2020. DOI: [10.1021/acsnano.9b09839](https://doi.org/10.1021/acsnano.9b09839).
- [17] P. Kim, L. Shi, A. Majumdar, and P. L. McEuen, "Thermal transport measurements of individual multiwalled nanotubes," *Phys. Rev. Lett.*, vol. 87, 2001. DOI: [10.1103/PhysRevLett.87.215502](https://doi.org/10.1103/PhysRevLett.87.215502).
- [18] L. Shi *et al.*, "Measuring thermal and thermoelectric properties of one-dimensional nanostructures using a microfabricated device," *J. Heat Transfer*, vol. 125, pp. 881, 2003. DOI: [10.1115/1.1597619](https://doi.org/10.1115/1.1597619).
- [19] Q.-Y. Li *et al.*, "Measurement of specific heat and thermal conductivity of supported and suspended graphene by a comprehensive Raman optothermal method," *Nanoscale*, vol. 9, pp. 10784–10793, 2017. DOI: [10.1039/C7NR01695F](https://doi.org/10.1039/C7NR01695F).
- [20] R. Wang, *et al.*, "Distinguishing optical and acoustic phonon temperatures and their energy coupling factor under photon excitation in Nm 2D materials," *Adv. Sci.*, vol. 7, pp. 2000097, 2020. DOI: [10.1002/adv.202000097](https://doi.org/10.1002/adv.202000097).
- [21] S. Xu, T. Wang, D. Hurley, Y. Yue, and X. Wang, "Development of time-domain differential Raman for transient thermal probing of materials," *Opt. Express*, vol. 23, pp. 10040, 2015. DOI: [10.1364/OE.23.010040](https://doi.org/10.1364/OE.23.010040).
- [22] P. Yuan, R. Wang, H. Tan, T. Wang, and X. Wang, "Energy transport state resolved Raman for probing interface energy transport and hot carrier diffusion in few-layered  $\text{MoS}_2$ ," *ACS Photonics*, vol. 4, pp. 3115–3129, 2017. DOI: [10.1021/acsp Photonics.7b00815](https://doi.org/10.1021/acsp Photonics.7b00815).
- [23] S. Xu, A. Fan, H. Wang, X. Zhang, and X. Wang, "Raman-based nanoscale thermal transport characterization: a critical review," *Int. J. Heat Mass Transfer*, vol. 154, pp. 119751, 2020. DOI: [10.1016/j.ijheatmasstransfer.2020.119751](https://doi.org/10.1016/j.ijheatmasstransfer.2020.119751).
- [24] R. Wang, T. Wang, H. Zobeiri, D. Li, and X. Wang, "Energy and charge transport in 2D atomic layer materials: Raman-based characterization," *Nanomaterials*, vol. 10, pp. 1807, 2020. DOI: [10.3390/nano10091807](https://doi.org/10.3390/nano10091807).
- [25] T. Wang, S. Xu, D. H. Hurley, Y. Yue, and X. Wang, "Frequency-resolved Raman for transient thermal probing and thermal diffusivity measurement," *Opt. Lett.*, vol. 41, pp. 80, 2016. DOI: [10.1364/OL.41.00080](https://doi.org/10.1364/OL.41.00080).
- [26] A. K. Vallabhaneni, D. Singh, H. Bao, J. Murthy, and X. Ruan, "Reliability of Raman measurements of thermal conductivity of single-layer graphene due to selective electron-phonon coupling: a first-principles study," *Phys. Rev. B*, vol. 93, pp. 125432, 2016. DOI: [10.1103/PhysRevB.93.125432](https://doi.org/10.1103/PhysRevB.93.125432).
- [27] S. Sullivan, *et al.*, "Optical generation and detection of local nonequilibrium phonons in suspended graphene," *Nano Lett.*, vol. 17, pp. 2049–2056, 2017. DOI: [10.1021/acs.nanolett.7b00110](https://doi.org/10.1021/acs.nanolett.7b00110).
- [28] G. Lucazeau, "Effect of pressure and temperature on Raman spectra of solids: anharmonicity," *J. Raman Spectrosc.*, vol. 34, pp. 478–496, 2003. DOI: [10.1002/jrs.1027](https://doi.org/10.1002/jrs.1027).
- [29] T. Beechem, A. Christensen, S. Graham, and D. Green, "Micro-Raman thermometry in the presence of complex stresses in GaN devices," *J. Appl. Phys.*, vol. 103, pp. 124501, 2008. DOI: [10.1063/1.2940131](https://doi.org/10.1063/1.2940131).
- [30] T. Beechem, S. Graham, S. P. Kearney, L. M. Phinney, and J. R. Serrano, "Invited article: simultaneous mapping of temperature and stress in microdevices using micro-Raman spectroscopy," *Rev. Sci. Instrum.*, vol. 78, pp. 061301, 2007. DOI: [10.1063/1.2738946](https://doi.org/10.1063/1.2738946).
- [31] K. R. Bagnall, E. A. Moore, S. C. Badescu, L. Zhang, and E. N. Wang, "Simultaneous measurement of temperature, stress, and electric field in GaN HEMTs with micro-Raman spectroscopy," *Rev. Sci. Instrum.*, vol. 88, pp. 113111, 2017. DOI: [10.1063/1.5010225](https://doi.org/10.1063/1.5010225).
- [32] M. T. Pettes, J. Maassen, I. Jo, M. S. Lundstrom, and L. Shi, "Effects of surface band bending and scattering on thermoelectric transport in suspended bismuth telluride nanoplates," *Nano Lett.*, vol. 13, pp. 5316–5322, 2013. DOI: [10.1021/nl402828s](https://doi.org/10.1021/nl402828s).
- [33] C. Wang *et al.*, "In situ Raman spectroscopy of topological insulator  $\text{Bi}_2\text{Te}_3$  films with varying thickness," *Nano Res.*, vol. 6, pp. 688–692, 2013. DOI: [10.1007/s12274-013-0344-4](https://doi.org/10.1007/s12274-013-0344-4).
- [34] Y. Wang, B. Qiu, A. J. H. McGaughey, X. Ruan, and X. Xu, "Mode-wise thermal conductivity of bismuth telluride," *J. Heat Transfer*, vol. 135, pp. 091102, 2013. DOI: [10.1115/1.4024356](https://doi.org/10.1115/1.4024356).
- [35] H. Goldsmid, "The thermal conductivity of bismuth telluride," *Proc. Phys. Soc. B*, vol. 69, pp. 203–209, 1956. DOI: [10.1088/0370-1301/69/2/310](https://doi.org/10.1088/0370-1301/69/2/310).
- [36] K. N. R. Taylor, "Thermal expansion of bismuth telluride," *Br. J. Appl. Phys.*, vol. 12, pp. 717, 1961. DOI: [10.1088/0508-3443/12/12/132](https://doi.org/10.1088/0508-3443/12/12/132).
- [37] D. Teweldebrhan, V. Goyal, and A. A. Balandin, "Exfoliation and characterization of bismuth telluride atomic quintuples and quasi-two-dimensional crystals," *Nano Lett.*, vol. 10, pp. 1209–1218, 2010. DOI: [10.1021/nl903590b](https://doi.org/10.1021/nl903590b).
- [38] J. P. Heremans, R. J. Cava, and N. Samarth, "Tetradymites as thermoelectrics and topological insulators," *Nat. Rev. Mater.*, vol. 2, pp. 17049, 2017. DOI: [10.1038/natrevmats.2017.49](https://doi.org/10.1038/natrevmats.2017.49).
- [39] P. W. Bridgman, "Certain physical properties of single crystals of tungsten, antimony, bismuth, tellurium, cadmium, zinc, and tin," *Proc. Am. Acad. Arts Sci.*, vol. 60, pp. 305, 1925. DOI: [10.2307/25130058](https://doi.org/10.2307/25130058).

- [40] C. R. Dean *et al.*, “Boron nitride substrates for high-quality graphene electronics,” *Nat. Nanotechnol.*, vol. 5, pp. 722–726, 2010. DOI: [10.1038/nnano.2010.172](https://doi.org/10.1038/nnano.2010.172).
- [41] S. Bertolazzi, J. Brivio, and A. Kis, “Stretching and breaking of ultrathin MoS<sub>2</sub>,” *ACS Nano*, vol. 5, pp. 9703–9709, 2011. DOI: [10.1021/nn203879f](https://doi.org/10.1021/nn203879f).
- [42] F. Bonaccorso, *et al.*, “Production and processing of graphene and 2D crystals,” *Mater. Today*, vol. 15, pp. 564–589, 2012.
- [43] L. M. Pavlova, Y. I. Shtern, and R. E. Mironov, “Thermal expansion of bismuth telluride,” *Teplofiz. Vysok. Temp.*, vol. 49, pp. 379–389, 2011.
- [44] S. P. Timoshenko and J. M. Gere, *Theory of Elastic Stability*. Courier Corporation, North Chelmsford, Chelmsford, MA, 2009.
- [45] E. Lund and T. G. Finstad, “Design and construction of a four-point bending based set-up for measurement of piezoresistance in semiconductors,” *Rev. Sci. Instrum.*, vol. 75, pp. 4960–4966, 2004. DOI: [10.1063/1.1808917](https://doi.org/10.1063/1.1808917).
- [46] W. Wu *et al.*, “Giant mechano-optoelectronic effect in an atomically thin semiconductor,” *Nano Lett.*, vol. 18, pp. 2351–2357, 2018. DOI: [10.1021/acs.nanolett.7b05229](https://doi.org/10.1021/acs.nanolett.7b05229).
- [47] L. Zhang *et al.*, “Thermal expansion coefficient of monolayer molybdenum disulfide using micro-Raman spectroscopy,” *Nano Lett.*, vol. 19, pp. 4745–4751, 2019. DOI: [10.1021/acs.nanolett.9b01829](https://doi.org/10.1021/acs.nanolett.9b01829).
- [48] B.-L. Huang and M. Kaviany, “Ab initio and molecular dynamics predictions for electron and phonon transport in bismuth telluride,” *Phys. Rev. B*, vol. 77, pp. 125209, 2008. DOI: [10.1103/PhysRevB.77.125209](https://doi.org/10.1103/PhysRevB.77.125209).
- [49] J. Kaiser, *et al.*, “Thermal transport at the nanoscale: a Fourier’s law vs. phonon Boltzmann equation study,” *J. Appl. Phys.*, vol. 121, pp. 044302, 2017. DOI: [10.1063/1.4974872](https://doi.org/10.1063/1.4974872).